

Volume: 09 Issue: 10 | Oct - 2025 SJIF Rating: 8.586 ISSN: 2582-3930

Reactive Power Optimization Approach for Hybrid AC/DC Networks Incorporating Multiple Wind Power Levels

Shaik Rizwan¹

¹PG student/Dept. of EPS, PVKK Institute of Technology, Andhra Pradesh, India

Abstract - As more wind power is integrated into the grid and AC/DC hybrid power systems continue to grow, voltage stability—especially at the receiving end—has become a serious concern. One effective way to address this issue is by using dynamic reactive power compensation devices. This paper introduces a strategy for optimizing reactive power in AC/DC hybrid grids, specifically taking into account the challenges introduced by renewable energy sources. It begins by developing a detailed mathematical model of the hybrid system. To improve voltage recovery after faults, the paper defines a new indicator to measure recovery performance. Based on this, an optimal control strategy for reactive power devices is created to boost the system's ability to bounce back from disturbances. Given the complex and nonlinear nature of the problem, the authors use a combination of the trajectory sensitivity method and the whale optimization algorithm to efficiently find solutions. The proposed method is then tested on an enhanced IEEE-9 system to verify its performance and practicality.

Key Words: Wind Power integration, AC/DC hybrid grids, Voltage Stability issues, Reactive power compensation, Optimization strategy, Renewable energy integration, Voltage recovery after faults, Trajectory sensitivity method, Whale optimization algorithm.

1.INTRODUCTION

India's energy resources and demand are unevenly distributed. Most wind and solar power plants are located in the northwest, while major electricity consumption centers lie in the developed eastern coastal areas. To balance this gap, long-distance, high-capacity ultra-high-voltage direct current (UHVDC) transmission systems are used to carry renewable energy to these load centers. Among these, LCC-HVDC systems are widely adopted due to their large transmission capacity, long-distance efficiency, and flexible construction.

When LCC-HVDC systems connect multiple regional grids, converter stations consume a large amount of reactive power—typically 40–60% during normal operation. After system faults, this reactive power demand rises sharply, leading to voltage instability at the receiving end. The issue is worse in remote areas where renewable power stations are built, as the grid there is usually weak and has low short-circuit capacity. Additionally, the replacement of traditional generators by DC input reduces local reactive power support, increasing the risk of commutation failures and voltage instability.

To address this, dynamic reactive power devices such as STATCOMs, SVCs, and SVGs are installed near DC receiving stations to improve voltage recovery and stability after faults. However, improper control or overuse of these devices for steady-state voltage regulation can limit their ability to provide

reactive power during faults, increasing instability risks. Hence, optimizing the coordination and operation strategy of these devices is essential to maintain both steady-state and transient voltage stability.

Previous studies have explored various control strategies for reactive power regulation in hybrid AC/DC systems. Literature [7] suggested an AVC substation control method, but it caused frequent mode switching under voltage fluctuations, reducing system stability. To improve this, [8] refined the AVC strategy by analyzing the excitation system of synchronous condensers. Another study [9] introduced a unified AVC control approach that integrates synchronous condensers, though it did not consider the effect on AC filters or parallel capacitors in converter stations. Later works [10] and [11] combined the control of condensers and AC filters, effectively using dynamic reactive devices for fast voltage regulation, which improved grid reliability.

Studies [12] and [13] highlighted that Doubly Fed Induction Generators (DFIGs) can independently manage active and reactive power by adjusting rotor excitation. Unlike conventional generators, DFIGs generate excitation through their rotor circuit, enabling them to supply reactive power to the grid via converters.

Further, [14] proposed a steady-state control strategy allowing synchronous condensers and AC filters to coordinate through information exchange between the AVC substation and DC control system. This reduced the number of AC filters required. However, [15] did not analyze how grid faults affect the transient performance of this coordination.

Overall, reactive power control in hybrid AC/DC networks is more complex than in traditional AC systems. Existing optimization goals mainly aim to minimize system losses or reactive power costs [16–19]. Some studies [20], [21] also included converter station loss characteristics and penalty functions for reactive power and voltage deviations to improve optimization accuracy.

Despite these advances, limited research focuses on how dispatchers can optimize the joint operation of multiple dynamic reactive devices to enhance both steady-state and transient voltage stability. This paper addresses that gap by introducing a fault recovery index as an optimization target. A quasi-steady-state model is used to describe the receiving-end HVDC converter station, and a Transient Stability Constrained Optimal Power Flow (TSCOPF) framework is developed. To efficiently solve the problem, trajectory sensitivity analysis and the whale optimization algorithm are applied, and the modified IEEE-9 bus system is used to verify the effectiveness of the proposed method.



Volume: 09 Issue: 10 | Oct - 2025 SJIF Rating: 8.586

2. Mathematical Modeling of the Hybrid **AC/DC Power System**

This section presents a quasi-steady-state mathematical model to describe the dynamic behavior of the receiving-end converter station (Section II-A). In an AC/DC hybrid grid, if the bus voltage fails to recover quickly after a short-circuit fault, it can disrupt DC operations, leading to commutation failures or even tripping, which threaten grid stability. Section II-B explains the transient model of the wind turbine generator system, while Section II-C focuses on the fault recovery process. n indicator is developed to evaluate and ensure the safe operation of the power

A. Quasi-Steady-State Mathematical Model of LCC-**HVDC**

The dynamic reactive power optimization model for the hybrid AC/DC receiving-end network can be expressed in a compact mathematical form as follows:

$$\min C(\mathbf{y}_0, \mathbf{u}_0) \tag{1}$$

$$s.t. \, \mathbf{g}_0(\mathbf{y}_0, \, \mathbf{u}_0) = 0 \tag{2}$$

$$\Phi_s(\mathbf{y}_0, \mathbf{u}_0) \le 0 \tag{3}$$

$$\dot{x}_s(t) - f_s(x_s(t), y_s(t), u_0) = 0, \ t \in [T_0, T_{\text{end}}]$$
 (4)

$$g_s(x_s(t), y_s(t), u_0) = 0, t \in [T_0, T_{end}]$$
 (5)

$$\Phi_s(\mathbf{x}_s(t), \mathbf{y}_s(t), \mathbf{u}_0) \le 0, \ t \in [T_0, T_{\text{end}}]$$
 (6)

In this model, the subscripts "0" and "s" denote the system's and fault-state conditions, respectively. T_0 represents the fault initiation time, and T_{end} indicates the end of the transient process. The state variable vector x includes factors such as motor slip and generator excitation EMF, while the algebraic variable vector ycontains parameters like bus voltage magnitude and phase angle. The control vector urepresents adjustable variables, and $C(\cdot)$ denotes the objective

Equation (2) defines the steady-state power flow, (3) sets the steady-state control and algebraic constraints, (4) models the system's dynamic response, (5) describes transient power flow during fault recovery, and (6) ensures compliance with transient voltage safety limits.

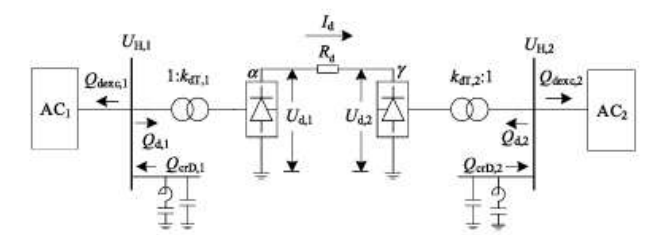


FIGURE 1. Schematic diagram of hybrid AC/DC transmission system.

Figure 1 presents a simplified schematic of the hybrid AC/DC transmission system. In this study, the operating characteristics of the LCC-HVDC system are represented using a quasisteady-state mathematical model, as expressed in equations (7)– (10).

$$U_{d,z} - \frac{3\sqrt{2}}{\pi} k_{b,z} k_{dT,z} U_{H,z} \cos \theta_z + \frac{3}{\pi} k_{b,z} X_{c,z} I_d = 0$$
 (7)

$$S_{d,z} - \frac{3\sqrt{2}}{\pi} k_{p,z} k_{b,z} \eta k_{dT,z} U_{H,z} I_d = 0$$
 (8)
$$S_{d,z}^2 - P_{d,z}^2 - Q_{d,z}^2 = 0$$
 (9)

$$S_{d,z}^2 - P_{d,z}^2 - Q_{d,z}^2 = 0 (9)$$

$$U_{d,z} = k_{p,z}U_{d,z}I_d$$
(10)

In this model, the subscript "z" takes values 1 and 2, referring to the sending-end and receiving-end converter stations, respectively. The converter control angle is denoted by $\theta_z(\alpha)$ for the rectifier and γ for the inverter). $k_{b,z}$ represents the number of six-pulse converters per pole, while $k_{p,z}$ indicates the number of operating poles. The commutation coefficient η is set to 0.995, and $X_{c,z}$ denotes the converter commutation reactance. $U_{d,z}$ is the DC voltage, while $S_{d,z}$, $P_{d,z}$, and $Q_{d,z}$ represent the apparent, active, and reactive power on the AC side of the converter transformer, respectively.

The rectifier operates under two control modes—constant current and constant firing angle—which can be expressed uniformly by equations (11)–(13). The binary variable x(0 or 1)identifies the control mode: x = 0 corresponds to the constant current mode, where $\alpha_{\min} \le \alpha \le \alpha_{\max}$, $I_{DC} = I_{DC,ref}$, $\gamma = \gamma_{ref}$; and x = 1 represents the constant firing angle mode, where $\alpha =$ α_{ref} , $I_{DC,\min} \leq I_{DC} \leq I_{DC,\max}$, $\gamma_{\min} \leq \gamma \leq \gamma_{\max}$. subscripts and overlines denote the lower and upper limits of each variable, respectively.

$$\underline{\alpha} \le \alpha \le \overline{\alpha} - (\overline{\alpha} - \underline{\alpha})x$$
 (11)

$$\frac{\underline{\alpha} \leq \underline{\alpha} \leq \overline{\alpha} - (\overline{\alpha} - \underline{\alpha})x}{I_{DC} - (I_{DC}) x \leq I_{DC} \leq I_{DC}} \tag{11}$$

$$\underline{\gamma} \leq \underline{\gamma} \leq \underline{\gamma} + (\overline{\gamma} - \underline{\gamma})x \tag{13}$$

$$\underline{\gamma} \le \underline{\gamma} \le \underline{\gamma} + (\overline{\gamma} - \underline{\gamma})x$$
 (13)

B. Dynamic Model of the Doubly-Fed Induction Generator (DFIG)

The Doubly-Fed Induction Generator (DFIG) offers several advantages over other wind turbine systems. It maintains high efficiency even at low wind speeds, expanding its operational range and improving energy utilization. DFIGs also handle grid disturbances well, making them suitable for power system integration. Their low starting current allows smooth operation at lower wind speeds, and their adaptability ensures stable performance under changing wind and load conditions. With lower maintenance costs and the ability to regulate power factor, DFIGs enhance grid stability and reliability. Owing to these benefits, DFIG technology is widely adopted for modern wind turbine systems. The transient behavior of such a system can be represented using the following mathematical model.

In this model, the state, algebraic, and control variables are follows:

$$x_{wind} = [\psi_{sd}, \psi_{sq}, \psi_{rd}, \psi_{rq}, \omega_t]^T,$$

$$y_{wind} = [i_{sd}, i_{sq}, i_{rd}, i_{rq}, T_e]^T,$$
 and

$$u_{wind} = [u_{sd}, u_{sq}, u_{rd}, u_{rq}, T_L]^T,$$

representing the state variables, algebraic variables, and control variables, respectively.

© 2025, IJSREM https://ijsrem.com



Volume: 09 Issue: 10 | Oct - 2025 SJIF Rating: 8.586

$$\begin{cases} \dot{x}_{\text{wind}} = ax_{\text{wind}} + by_{\text{wind}} + cu_{\text{wind}} \\ 0 = dx_{\text{wind}} + ey_{\text{wind}} + fu_{\text{wind}} \end{cases}$$
(14)

$$\mathbf{a} = \begin{bmatrix} 0 & w_s w_b & 0 & 0 & 0 \\ -w_s w_b & 0 & 0 & 0 & 0 \\ 0 & 0 & 0 & w_s w_b & 0 \\ 0 & 0 & -w_s w_b & 0 & 0 \\ 0 & 0 & 0 & 0 & 0 \end{bmatrix}$$
(15)
$$\mathbf{b} = diag \left(-w_b R_s & -w_b R_s & -w_b R_r & -w_b R_r & -\frac{n_p}{J} \right)$$

$$\mathbf{b} = \operatorname{diag} \left(-w_b R_s - w_b R_r - w_b R_r - \frac{n_p}{J} \right)$$

$$\mathbf{c} = \operatorname{diag} \left(w_b - w_b - w_b - \frac{n_p}{J} \right) \tag{16}$$

$$\mathbf{d} = \operatorname{diag} \begin{pmatrix} -1 & -1 & -1 \\ \end{pmatrix} \tag{17}$$

$$e = 0 (18)$$

$$f = \begin{bmatrix} 0 & X_s + X_m & 0 & X_m \\ X_s + X_m & 0 & X_m & 0 \\ 0 & X_m & 0 & X_r + X_m \\ X_m & 0 & X_r + X_m & 0 \end{bmatrix}$$
(19)

In modern power systems, the concept of elasticity has emerged as a key measure to evaluate a grid's ability to withstand disturbances, respond quickly during faults, and recover efficiently afterward. To assess this, two main factors are considered: the recovery time of the AC bus voltage to its minimum stable level and the number of commutation failures that occur during the process. Based on these parameters, a Fault Recovery Indicator (FRI) is proposed to evaluate voltage elasticity, expressed as:

$$FRI_{v} = \frac{1}{N_{f}} \sum_{i=1}^{N_{f}} FRI_{v,i} = \frac{1}{N_{f}} \sum_{i=1}^{N_{f}} e^{-\frac{T_{i}}{T_{\text{max}}} - \frac{N_{i}}{N_{\text{max}}}}$$
(20)

Here, FRI_v denotes the voltage elasticity coefficient of the system, and N_f is the number of short-circuit faults on nearby AC transmission lines. The term irepresents the sequence number of each fault. T_{max} is the maximum permissible duration for which voltage can remain below U_s during a fault, while N_{max} indicates the highest allowable number of commutation failures before DC blocking. T_i is the time taken for the AC bus voltage at the converter station to recover to U_safter the i-th fault, and N_i represents the corresponding number of commutation failures. U_s is the minimum voltage required to ensure stable AC bus operation, as defined by system standards. In practice, DC lines are electrically far apart, meaning faults in one region have minimal influence on others. Therefore, the FRI index is evaluated based on the voltage and arc extinction angle characteristics of a single DC line within its local grid. By accounting for both the voltage recovery duration and the number of commutation failures, the FRI reflects the grid's resilience against faults. The value of FRI_{ν} ranges from (0, 1], where a higher value indicates faster voltage recovery and stronger system resilience.

III. Optimal Scheduling Strategy for Dynamic Reactive **Power Devices**

This section presents an optimal scheduling framework for dynamic reactive power devices. The detailed mathematical model is developed in Section III-A. Since the optimization problem essentially represents a Transient Stability Constrained Optimal Power Flow (TSCOPF) problem, numerous transient constraints described by differential equations must be considered. To address this, the trajectory sensitivity method is used in Section III-B to transform the TSCOPF model into a Steady-State Constrained Optimal Power Flow (SCOPF)

problem. Furthermore, because the model is nonlinear and nonconvex (a Mixed-Integer Nonlinear Programming problem, MINLP), the Whale Optimization Algorithm (WOA) is applied in Section III-C to improve computational efficiency and ensure effective solution convergence.

A. Formulation of the Optimal Scheduling Strategy

The objective of the optimal scheduling strategy for dynamic reactive power compensation devices is to maximize the Fault Recovery Indicator (FRI), as expressed in equation (21).

$$obj = \max FRI_V \tag{21}$$

At the same time, several constraints must be considered in the optimization process. These include limits on reactive power output, power flow, voltage levels, phase angles, and transient stability conditions. Both dynamic and static reactive power compensation devices are required to meet the constraints defined in equations (22)–(23).

$$Q_{\min,l} \le Q_l^d \le Q_{\max,l} \tag{22}$$

$$K_{\min} \le K \le K_{\max}$$
 (23)

Here, $Q_{d,l}$ denotes the steady-state reactive power output of the dynamic device, while $Q_{max,l}$ and $Q_{min,l}$ represent its upper and lower output limits, respectively. Kindicates the number of static reactive power compensation devices (such as capacitor banks) in operation.

Additionally, the AC system must comply with the power flow equations (24)–(25), as well as the node voltage constraints (26) and phase angle constraints (27).

$$\Delta P_i = P_{Gi} - P_{Li} \pm P_{di} - U_i \sum_j U_j (G_{ij} \cos \theta_{ij} + B_{ij} \sin \theta_{ij})$$
(24)

$$\Delta Q_i = Q_{Gi} - Q_{Li} \pm Q_{di} - U_i \sum U_j (G_{ij} \sin \theta_{ij} - B_{ij} \cos \theta_{ij})$$
(25)

$$U_{\min,i} \le U_i \le U_{\max,i} \tag{26}$$

$$\delta_{\min,i} \le \delta_i \le \delta_{\max,i}$$
 (27)

B. Trajectory Sensitivity Analysis Method

Due to the necessity of considering transient-related constraints at the receiving end during fault conditions, a large number of differential-algebraic equations (DAEs) are introduced into the optimization problem, which significantly increases the computational complexity. To address this challenge, the trajectory sensitivity method is employed to transform the initial Transient Security Constrained Optimal Power Flow (TSCOPF) model into a standard Security Constrained Optimal Power Flow (SCOPF) formulation.

First, the differential-algebraic equations for the receiving end

$$\begin{cases} \dot{x} = f(x, y, u, t) \\ 0 = g(x, y, u, t) \end{cases}$$

where xrepresents the state variables, ydenotes the algebraic variables, urefers to the control variables, and tis the time variable.



Volume: 09 Issue: 10 | Oct - 2025 SJIF Rating: 8.586 ISSN: 2582-3930

$$0 = g^s(x, y, u) \tag{29}$$

$$0 = g^{s,c}(x, y, u) \tag{30}$$

Here, the superscript "s" denotes the fault occurrence, while "c" represents the fault clearance instant. Meanwhile, the system's state variables must satisfy the constraint expressed in equation (31):

$$x^c = \phi(x^s, t^c - t^s)$$

Here, t_0 denotes the moment when the fault occurs, while t_0^- and t_0^+ represent the instants immediately before and after the fault, respectively. The terms x_{t0^-u} and x_{t0^+u} indicate the partial derivatives of the initial state variables with respect to the control variables before and after the fault occurrence.

$$y_u^{t_0^+} = -(g_y^{s,t_0^+})^{-1} g_u^{s,t_0^+}$$
 (32)

$$x_u^{t_c^+} = x_u^{t_c^-} \tag{33}$$

$$y_u^{t_c^+} = -(g_y^{s,c,t_c^+})^{-1} g_u^{s,c,t_0^+}$$
(34)

$$\begin{bmatrix} x_{u}^{T+1} \\ y_{u}^{T+1} \end{bmatrix} = J^{-1} \begin{bmatrix} (I + \frac{h}{2} f_{x}^{T}) x_{u}^{T} + \frac{h}{2} f_{x}^{T} y_{u}^{T} \\ + \frac{h}{2} (f_{u}^{T+1} + f_{u}^{T}) \\ \frac{h}{2} g_{x}^{T} x_{u}^{T} + \frac{h}{2} g_{y}^{T} y_{u}^{T} + \frac{h}{2} (g_{u}^{T+1} + g_{u}^{T}) \end{bmatrix}$$
(35)

C. Solution Algorithm - Whale Optimization Algorithm

1) Encircling Prey

In the Whale Optimization Algorithm (WOA), the prey's position represents the approximate optimal solution. Since the exact location of the prey (optimum) is unknown, the algorithm first identifies the best current solution, treating it as the prey. The remaining whales then update their positions around this optimal candidate. This behavior is mathematically modeled using equations (36)–(39).

$$D = |C \cdot X^*(e) - X(e)| \tag{36}$$

$$X(e+1) = X^*(e) - A \cdot D$$
 (37)

$$A = 2ar - a \tag{38}$$

$$C = 2r \tag{39}$$

2) Bubble-Net Attacking

In this stage, whales approach the prey using two mechanisms: contraction encircling and spiral updating. The contraction encircling process is controlled by the parameter a, with A randomly varying between (-2, 2) based on a and r. In the spiral updating process, a spiral path is formed between the whale and the prey by calculating their distance. The resulting spiral motion is described by equations (40)–(41).

$$X(e+1) = D^{\times} e^{bl} \cos(2\pi l) + X^{*}(e)$$
 (40)

$$D^{\times} = |X^{*}(e) - X(e)| \tag{41}$$

$$D = |C \cdot X_{rand}(t) - X(t)| \tag{42}$$

$$X(t+1) = X_{rand}(t) - A \cdot D \tag{43}$$

IV. CASE STUDY

To verify the effectiveness and feasibility of the proposed method, simulations were conducted on the improved IEEE-9-bus and IEEE-39-bus test systems, each containing a DC subsystem. The detailed network configurations are shown in Figures 3 and 4.

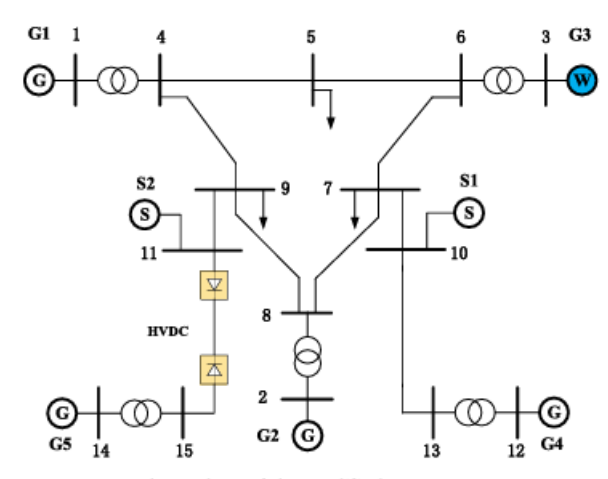


FIGURE 3. Network topology of the modified IEEE-9 test system.

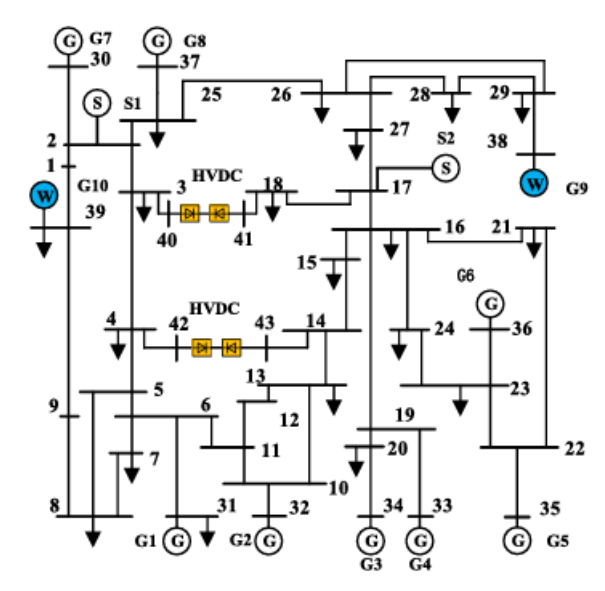
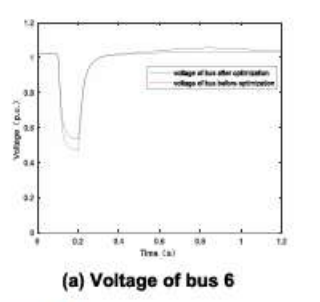


FIGURE 4. Network topology of the modified IEEE-39 test system.

From the analysis, it is evident that the DC system behaves as a reactive power load for the receiving-end AC grid. The fault recovery process varies with wind power penetration. As wind penetration increases, system stability decreases, requiring more dynamic reactive power support during faults. After a fault, the DC system draws significant reactive power from the AC grid, temporarily increasing the reactive load and slowing voltage recovery. This weakens the system's stability margin. If the induction motor's slip surpasses the critical value when the fault clears, transient voltage instability can occur due to negative voltage—reactive power feedback. Essentially, system instability arises from an imbalance in reactive power, which can be mitigated by adding compensation at the DC converter bus.



Volume: 09 Issue: 10 | Oct - 2025 SJIF Rating: 8.586 ISSN: 2582-3930



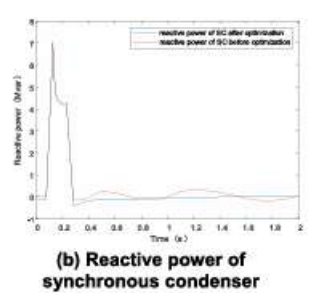
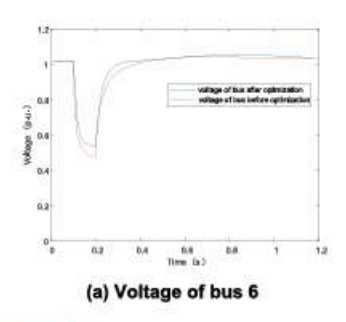


FIGURE 5. The voltage recovery situation at the busbar before and after optimization with a wind power penetration rate of 10% in improved IEEE-9 node testing system.



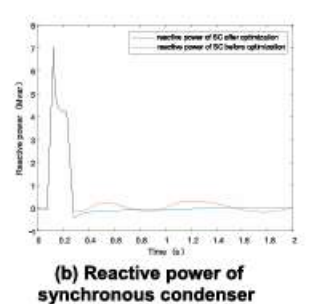
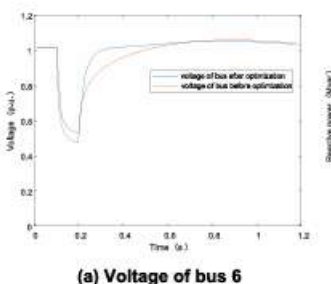


FIGURE 6. The voltage recovery situation at the busbar before and after optimization with a wind power penetration rate of 20% in improved IEEE-9 node testing system.



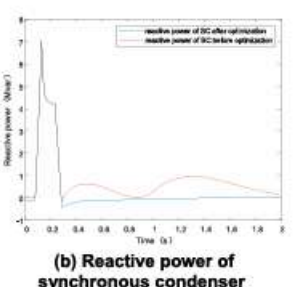


FIGURE 7. The voltage recovery situation at the busbar before and after optimization with a wind power penetration rate of 30% in improved IEEE-9 node testing system.

When reactive power compensation is provided at the DC converter bus after a fault, the reactive power deficit at the receiving end is alleviated, thereby improving the system's stability margin and enabling it to withstand more severe disturbances.

Figure 5 illustrates the voltage recovery performance of the buses under the proposed optimization method. It can be observed that, after optimization, Bus 6 exhibits a noticeable improvement in its voltage support capability and transient voltage recovery characteristics. Additionally, the stability of the static compensator (SC) reactive power output is significantly enhanced.

Figure 6 further demonstrates that, as the wind power penetration level increases, both the voltage–reactive power support capacity and the transient voltage recovery ability of Bus 6 improve correspondingly. The enhanced optimization also leads to greater stability in the SC reactive power output, confirming the robustness and adaptability of the proposed reactive power scheduling strategy under varying wind integration scenarios.

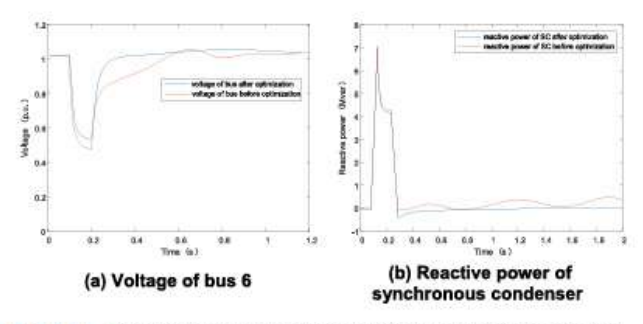
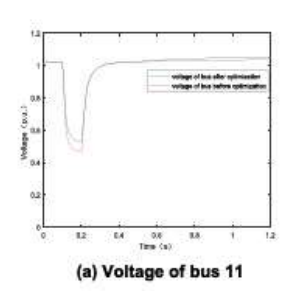


FIGURE 8. The voltage recovery situation at the busbar before and after optimization with a wind power penetration rate of 40% in improved IEEE-9 node testing system.



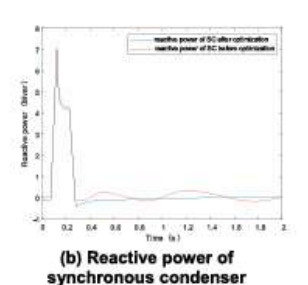
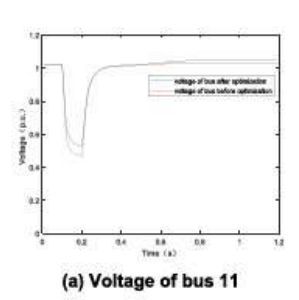


FIGURE 9. The voltage recovery situation at the busbar before and after optimization with a wind power penetration rate of 10% in improved IEEE-39 node testing system.



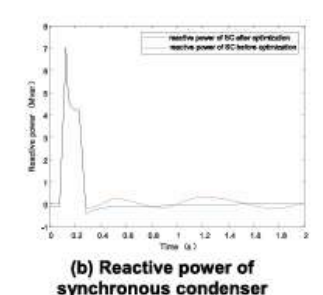


FIGURE 10. The voltage recovery situation at the busbar before and after optimization with a wind power penetration rate of 20% in improved IEEE-39 node testing system.

From Figure 7, it is observed that as the wind power penetration rate increases, Bus 6 shows a significant improvement in both its voltage-reactive power support capacity and transient voltage recovery performance. Additionally, the stability of the static compensator (SC) reactive power output is notably enhanced.

Similarly, Figure 8 illustrates that after optimization, Bus 6 experiences a substantial boost in its reactive power support capability and a marked enhancement in transient voltage recovery. The stability of the SC reactive power output also improves considerably, highlighting the effectiveness of the proposed optimization approach.

As shown in Figure 9, Bus 11 demonstrates a modest increase in its voltage-reactive power support capacity following optimization, along with a slight improvement in transient voltage recovery ability, indicating consistent benefits across different buses in the system.

Figure 9 shows that Bus 11 experiences a moderate improvement in its transient voltage recovery performance, along with enhanced stability of the SC reactive power output after optimization.

As seen in Figure 10, with the increase in wind power penetration, Bus 11 demonstrates a significant boost in its voltage-reactive power support capacity and a clear



Volume: 09 Issue: 10 | Oct - 2025 SJIF Rating: 8.586 ISSN: 2582-3930

improvement in its **transient voltage recovery ability**. Additionally, the **stability of the SC reactive power output** is notably strengthened, further validating the positive impact of the proposed optimization strategy.

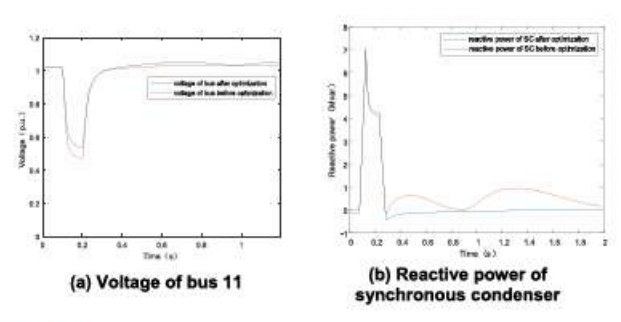


FIGURE 11. The voltage recovery situation at the busbar before and after optimization with a wind power penetration rate of 30% in improved IEEE-39 node testing system.

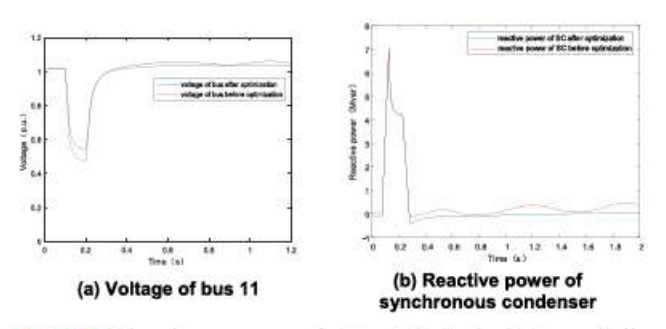
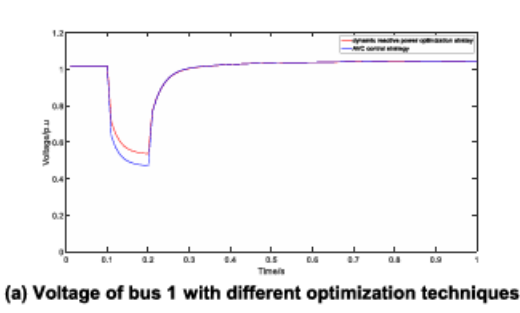
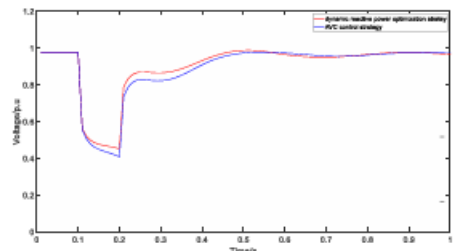


FIGURE 12. The voltage recovery situation at the busbar before and after optimization with a wind power penetration rate of 40% in improved IEEE-39 node testing system.





(b) Voltage of bus 8 with different optimization techniques

FIGURE 13. The Influence of dynamic reactive power optimization strategy and AVC control strategy on buses.

Figure 13 presents a comparison between the effectiveness of the proposed optimization method and the conventional approach. This comparison highlights the superior performance of the proposed method in enhancing voltage recovery, improving reactive power support, and maintaining overall system stability under fault conditions.

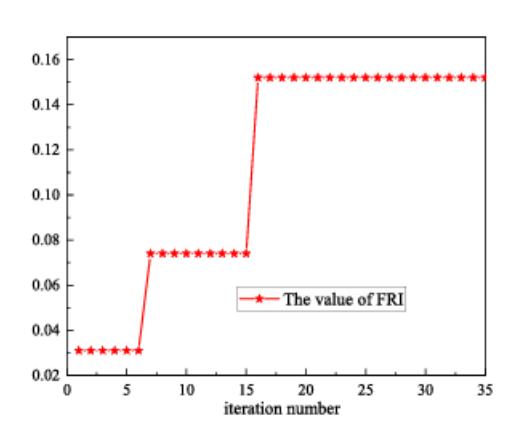


FIGURE 14. Convergence curve of the whale optimization algorithm.

TABLE 1. Dc control system parameters.

	T_{rc}	K_r	T_r	V_D^m	V_D^M	I_D^m
Commutating	0.005	0.10	0.02	0.4	0.9	0.5
side	I_D^M	$lpha^{\!\scriptscriptstyle{ ext{min}}}$	$lpha^{\min}$			
	1.0	5°	110°			
	T_{ic}	K_{i1}	T_{i1}	K_{i2}	T_{i2}	$oldsymbol{eta}_{\!\!1}^{\!$
	T _{ic} 0.005	<i>K</i> _{i1} 0.10				$oldsymbol{eta_l^{min}}$ 90°
Inverse side						β ₁ ^{min} 90°

In conclusion, the synchronous condenser (SC) provides rapid reactive power support by quickly entering a strong excitation state when the system voltage drops after a fault. This immediate response helps reduce the risk of DC commutation failure. Additionally, the SC adjusts effectively to system voltage and reactive power demands, enabling faster recovery of both DC and AC system voltages and enhancing transient stability. Furthermore, generators in the system generally contribute positively to converter bus voltage stability, as their additional reactive power during transients strengthens system resilience. However, in some cases, increased generator reactive output during faults can negatively affect recovery by limiting reactive support from other generators that are more closely coupled with the DC system.

At the converter bus, reduced voltage support from the receiving end can cause deeper voltage dips and slower recovery. From an operational standpoint, increasing the reactive power reserve of generators enhances the voltage stability of multi-DC-fed systems and strengthens their ability to handle disturbances.

Conventional dynamic reactive power optimization models are complex, as they include numerous transient constraints and are typically non-convex mixed-integer nonlinear programming (MINLP) problems, which are difficult to solve efficiently. To address this challenge, this study employs the Whale Optimization Algorithm (WOA) to simplify and accelerate the computation process. Figure 5 illustrates the convergence curve of the WOA, where the initial optimal objective value is 0.031, demonstrating the algorithm's capability to efficiently reach improved solutions.



Volume: 09 Issue: 10 | Oct - 2025 SJIF Rating: 8.586 ISSN: 2582-3930

TABLE 2. Converter station parameters.

	Active power/ MW	Convert er reactive power /Mvar	Filter capacity /Mvar	Commu tating reactan ce /p.u.	Trigger Angle/q uenchin g Angle
Commut ating side converter station 1	68.96	28.90	10	0.1	13.17°
Commut ating side converter station 2	49.29	18.08	10	0.1	14.25°
Inverter side converter station 1	65.43	36.06	10	0.1	20°
Inverter side converter station 2	46.84	23.35	10	0.1	20°

TABLE 3. Generator/modulator and its excitation system parameters.

	X_d	X_d'	X_d^{σ}	T_{d0}'	T_{d0}^{r}	X_q	X_q'	X_q^{r}
G1	1.80	0.30	0.25	8.0	0.03	1.70	0.55	0.24
G2	1.80	0.30	0.25	8.0	0.03	1.70	0.55	0.24
G3	1.80	0.30	0.25	8.0	0.03	1.70	0.55	0.24
G4	1.80	0.30	0.25	8.0	0.03	1.70	0.55	0.24
G5	1.80	0.30	0.25	8.0	0.03	1.70	0.55	0.24
S1	1.50	0.20	0.15	6.0	0.02	1.60	0.50	0.20
S2	1.50	0.20	0.15	6.0	0.02	1.60	0.50	0.20

1.Dynamic reactive power devices, especially synchronous condensers, greatly enhance system voltage recovery. Compared to static devices, the proposed optimization approach provides faster voltage restoration and reduces the likelihood of continuous commutation failures.

2. The integration of trajectory sensitivity analysis with the Whale Optimization Algorithm (WOA) significantly boosts computational efficiency, making the method suitable for real-time online applications.

Looking ahead, with the growing share of renewable energy and higher wind power penetration, incorporating advanced and robust control strategies will further improve voltage stability and system performance. Since long-term wind power fluctuations can affect reactive power reserve planning, future research will focus on considering wind power prediction errors and related system variables, along with the influence of increasing generator output on system optimization.

Future work will also address the **uncertainty in wind power generation**. The random fluctuations in wind output can lead to variations in the number of operating generation units and affect system stability. To handle this, a **robust optimal reactive power optimization model** will be developed, which accounts for **wind power randomness** while ensuring **system security constraints** are satisfied. This model aims to maintain reliable

voltage stability and optimal reactive power distribution even under uncertain renewable energy conditions.

References:

[1]N.Chen,K.Zha,H.Qu,F.Li,Y.Xue,andX.-

P.Zhang, "Economyanalysis of flexible LCC-HVDC systems with controllable capacitors," CSEE J. Power Energy Syst., vol. 8, no. 6, pp. 1708–1719, Nov. 2022.

[2] Y. Xue, X.-P. Zhang, and C. Yang, "AC filterless flexible LCC HVDC with reducedvoltagerating of controllable capacitors," IEEE Trans. Power Syst., vol. 33, no. 5, pp. 5507–5518, Sep. 2018.

[3] A. Omer, X. Wang, Z. Xie, and C. Li, "Analysis of commutation failure in LCC-HVDC systems during unbalanced conditions using sequence components," in Proc. Int. Conf. Power Syst. Technol. (POWERCON), Haikou, China, Dec. 2021, pp. 2404–2408.

[4]Y.Xue,C.Yang,andX.P.Zhang,"ReactivepowerandACvoltag esupport from flexible LCC HVDC to wind energy integrated power system," in Proc. AEIT Int. Annu. Conf. (AEIT), Catania, Italy, Sep. 2020, pp. 1–4.

[5] H. Li and K. Qin, "Comparative analysis of small signal stability of LCC HVDCsystemwith constant voltage control and constant extinction angle control," in Proc. 3rd Int. Academic Exchange Conf. Sci. Technol. Innov. (IAECST), Guangzhou, China, Dec. 2021, pp. 1758–1764.

[6] H. Xiao, X. Duan, Y. Zhang, and Y. Li, "Comparative analysis of inter inverter interactions in emerging hierarchical-infeed and conventional multi-infeed LCC-

BIOGRAPHIES



Name - Shaik Rizwan